Surface temperature and salinity in the northern Bay of Bengal: *in situ* measurements compared with satellite observations and model output

Md. Masud-Ul-Alam,[a,b,*] **Md. Ashif Imam Khan**,[a] **Bradford S. Barrett**,[c,d] **and Sara Rivero-Calle**[b]

[a]Bangabandhu Sheikh Mujibur Rahman Maritime University, Department of Oceanography and Hydrography, Dhaka, Bangladesh

[b]University of Georgia, Skidaway Institute of Oceanography, Department of Marine Sciences, Savannah, Georgia, United States

[c]U.S. Naval Academy, Oceanography Department, Annapolis, Maryland, United States

[d]Air Force Office of Scientific Research (AFOSR), Arlington, Virginia, United States

Abstract. The northern Bay of Bengal (BoB) has been traditionally understudied and undersampled. Satellite and modeling products could compensate for the scarcity of *in situ* measurements, but this requires evaluating the accuracy of satellite and modeling products first. We present a comparison of sea surface temperature (SST) and sea surface salinity (SSS) products (satellite and model output) with 46 *in situ* observations in the northern BoB. We used satellite and modeled SST (daily) and SSS (weekly and daily) in this comparison. The results are as follows. (1) Both model and satellite-derived SSTs agreed well with *in situ* observations and with each other, with small biases (<1°C) and large correlation coefficients ($r > 0.77$). (2) Neither model nor satellite SSSs agreed well with *in situ* observations (biases > 0.5 PSU, $r < 0.54$). (3) Calculations of the *d*-index support the argument that model and satellite SSTs agreed well with *in situ* observations (*d*-index values of 0.68 and 0.65, respectively), while the model and satellite SSSs did not agree well with observations (*d*-index values of 0.31 and 0.40, respectively). The results suggest that additional work is needed to improve both model prediction and satellite retrieval algorithms for SSS in the northern BoB. [DOI: 10.1117/1.JRS.16.018502]

Keywords: Bay of Bengal; sea surface temperature; sea surface salinity; *in situ* measurements; satellite observations; model output.

Paper 210423 received Jul. 8, 2021; accepted for publication Dec. 16, 2021; published online Jan. 5, 2022.

1 Introduction

Accurate and timely remote measurements of ocean temperature and salinity are essential for numerical prediction models[1] to forecast the ocean and atmosphere dynamics. Obtaining precise global sea surface temperature (SST) estimates has been the focus of the study of many groups for the last few decades. In a classical study, Brown et al.[2] analyzed calibration methods of the U.S. National Oceanographic and Atmospheric Administration (NOAA) Advanced Very High Resolution Radiometer (AVHRR), by deriving accurate SST fields from satellite infrared (IR) observations, based on vacuum test datasets. Similarly, Kumar et al.[3] explicitly examined the global Pathfinder algorithm's performance in regional conditions, by comparing satellite data to buoy data. They concluded that a variation of ∼5°C existed between these two sources. Recently, a saildrone instrument was used by Vazquez-Cuervo et al.[4] to study SST retrievals. Among the six different Group for High Resolution Sea Surface Temperature (GHRSST) Level-4 SST and Level-2 SSS products, they found good agreement with satellite-derived SST and less correlation to the SSS datasets.

*Address all correspondence to Md. Masud-Ul-Alam, masud.ocn@bsmrmu.edu.bd

Modern numerical ocean models capitalize on remote observations of temperature and salinity to help us understand both large- and small-scale processes in the Indian Ocean (IO). For example, Jensen et al.[5] used the global Hybrid Coordinate Ocean Model and the Regional Ocean Modeling System (ROMS) to illustrate exchanges of salinity between the Bay of Bengal (BoB) and the IO. Moreover, Benshila et al.[6] used the Nucleus for European Modeling of the Ocean (NEMO) system to provide one of the first a high-resolution structures of salinity in the BoB. Finally, important details on temperature inversions in the BoB were provided by Babu and Rao[7] using the Princeton Ocean Model. These examples show how useful it is for researchers to use model output to evaluate physical, chemical, and biological parameters in the IO.

Recent improvements in numerical modeling[8] and remote sensing (RS) systems include greater horizontal and vertical resolution and the introduction of new instruments, theories, and methodologies. Moreover, continuous monitoring of SST and sea surface salinity (SSS) is now possible over large spatial and temporal scales.[9] Even on days when the satellite measurements contain missing values, other available products, including aerial and drone photography, buoy measurements, conductivity, temperature, and depth (CTD) profiles, and water sample analyses, can be used to fill the gaps.[10] Indeed, high-resolution satellite-based observations of oceanographic fields,[11] along with their assimilation into numerical ocean prediction models,[12] enable advances in research and operational forecasting in marine sciences.[13] Both active and passive satellite scanning strategies can be utilized to acquire a variety of oceanic parameters, including suspended particulate matter (SPM),[14] sea surface roughness,[15] and wave height.[16] These satellite-derived products are very essential to the modeling study.

One way to evaluate numerical prediction model performance is to compare model output to satellite products.[17] The AVHRR product of the NOAA is one such scanning system that has been used since 1981 to determine ocean SST in near real time.[18] However, the use of satellite-derived SST has some associated caveats. Satellites measure the skin SST (at depth of ~10 to 20 μm), which is colder than the bulk SST (of the topmost few meters) by 0.1°C to 0.5°C.[19] In addition, it depends on whether the satellite is measuring emitted radiation in the IR or in the visible as an approximate solution to the radiative transfer equation. [20] Furthermore, there are some satellites (GHRSST) those measure at night and others measure during the beginning of the day initial when the heat buildup from absorption of solar radiation surpasses the heat loss at the sea surface (also known as foundation SST). This type of satellite-derived estimates with a diurnal correction provide SST with negligible (<0.05°C) biases.[21] Although there are different methods to estimate SST, scientists are consistently introducing new techniques to measure other parameters, such as SSS, from the space.

Remotely sensed observations of SSS are more recent and they are not as developed as SST. However, two platforms were recently launched: the Soil Moisture and Ocean Salinity (SMOS) satellite in 2009[22] and the launch of the joint U.S./Argentinian Aquarius/Satélite de Aplicaciones Científicas (SAC)-D satellite in 2011. Although Aquarius came to halt in 2015, the SMOS platform is still engaged in routine monitoring of SSS.

Widespread usage of model output and satellite observations leads to questions regarding their accuracy. One way to measure that accuracy is to compare RS data and model output to *in situ* observations, particularly for continental shelf regions where those observations are more common. However, *in situ* observations themselves have uncertainty,[23] and that possible error should be considered when making any comparisons. Nevertheless, a comparison of both model output and RS observations with *in situ* observations on similar spatial and temporal scales can give an estimate of the accuracy of both model output and RS data. This is particularly important in enclosed regions such as the BoB that feature high to extreme sediment inputs and freshwater discharges that can complicate satellite retrieval algorithms.

Noteworthy differences between satellite SST (hereafter abbreviated as SST_{sat}) products and *in situ* measurements of coastal water temperature (hereafter abbreviated as SST_{in}) have been noted in previous continental shelf studies in other parts of the world. For example, Castillo and Lima[24] found negative biases between *in situ* readings and Moderate Resolution Imaging Spectroradiometer (MODIS) SST_{sat} products in reef-dominated coastal waters in southern Belize. Additionally, large biases, up to 6°C, between *in situ* and RS measurements were detected in 87 sites spanning the South African coastline. Although smaller in magnitude, Wu et al.[25] found 1°C root mean square error (RMSE) for the Atlantic Zone Monitoring Program's

ship-based SST_{in} in the eastern Canadian shelf waters. That error was found when comparing the SST_{in} with operational SST analyses from both the Canadian Meteorological Centre and the U.S. National Centers for Environmental Prediction. Stobart et al.[26] found high correlations between annual SST_{in} and SST_{sat} for 32 stations in the southern Australia coastal region, but they noted significant seasonal and regional variability. Pramanik et al.[27] found significant correlations ($r = 0.78$) between ROMS and MODIS satellite observations at the Sri Lankan dome region, near the southern BoB. Furthermore, Lin et al.[28] compared the Aquarius SSS with ARGO *in situ* measurements and detected large negative biases in the northern BoB.

Differences between *in situ* (IS) observations, RS measurements, and numerical model output, particularly on regional and seasonal scales, make comparison studies crucial. It is generally accepted that remotely sensed measurements are well suited for large spatiotemporal scales (e.g., in the open ocean or on weekly to monthly time scales).[24,29] However, RS retrievals often perform poorly in the coastal shelf waters and on sub-weekly time scales. In these coastal shelf areas, SST and SSS products with horizontal grid spacing >1 km are unable to accurately capture all of the features located near the coastlines.[30] Coastal waters can be dynamic and unstable,[31] particularly where there are large riverine discharges. That is especially the case in the northern BoB because the Ganges–Brahmaputra river transports $\sim 1 \times 10^9$ tons $year^{-1}$ of sediment to the coast, ranking first (along with the Amazon outflow) among the world's estuaries and rivers in terms of sediment discharge.[32–35] The continental shelf of the northern BoB, especially from 21.5°N to 22.5°N, contains very high concentrations of total SPM, peaking at 95 kg m^{-3} in summer,[36] which is more than four orders of magnitude higher than in the open-ocean parts of the IO (0.06 kg m^{-3}).[37,38] The presence of SPM significantly reduces sea surface radiative emissivity of coastal water, thus disrupting the measurements of thermal radiometers that form the core of satellite-based RS.[39,40]

The presence of estuaries and rivers causes the sediment composition to be extremely complex.[41] Thus, the higher concentration of sediments in the northern BoB makes it more prone to these emission errors. The northeastern part of the continental shelf of the tropical IO is predominantly composed of low saline (10 to 15 PSU) surface water. These relatively low salinity values are the result of significant river water influxes as well as strong overturning from the seasonally dependent monsoon wind system.[42] The surface salinity is coupled with a marked annual cycle in SSTs.[43] When SSTs in the BoB are warm, there is more precipitation, and surface salinity is lower due to freshwater rain and river influx, again particularly in the continental shelf region.[44,45] The northern BoB tends to feature small-scale SSS boundaries in all four seasons.[46] This regional variability in SSS is due to advection-induced freshwater fluxes.[6] The relatively small scale of the SSS features indicates that detailed high-resolution modeling and RS products are needed to capture the salinity structure. However, comparisons between RS products, model output, and *in situ* measurements remain scarce, partly because of the scarcity of *in situ* measurements. Moreover, the fixed buoy network has degraded since about 2015,[47,48] and there is a lack of both research expeditions[49] and routine cruises to collect *in situ* physicochemical parameters.[50,51] Thus, studies such as this one are crucial to understand the surface salinity and temperature structure in the BoB.

Uncertainties of the regional application of the global model and satellite-derived SST and SSS are the key inspirations to do this study. The applications of such models are often problematic, especially on a regional scale.[52] The concern further escalates if the study region (e.g., BoB), lacks cruise-based observations[36] and is dependent on model or satellite measurements. Additionally, the presence of clouds, especially in the tropical region, limits some sensors' capabilities, resulting in data gaps.[9] These gaps suggest a continued need for *in situ* measurements. Finally, greater temporal and spatial coverage of *in situ* observations in the northern BoB, especially in the coastal shelf regions, would help to derive improved algorithms for satellite retrieval of SST and SSS. These improved retrieval algorithms could lead to improved model parameterizations in numerical models, allowing them to better capture important regional processes.

Accurate representation of both SST and SSS would thus improve both ocean and atmosphere numerical model skills.[53] Comparative studies such as this one are imperative, as these would provide critical justification for subsequent statistical adjustments to satellite SST and SSS retrieval algorithms, resulting in improved representation of regional and small-scale disturbances in the RS measurements. This study addresses two critical questions: (1) How do the

model and remotely sensed data differ from *in situ* observations? (2) What are the spatial and temporal biases in model output and satellite observations? The remainder of this article is organized as follows: the data and analytical methods are presented in Sec. 2. Results are presented in Sec. 3. Discussion and conclusions are presented in Secs. 4 and 5, respectively.

2 Materials and Methods

2.1 *Model Description*

Daily surface ocean analyses from the Copernicus Marine Environment Monitoring Service (CMEMS) NEMO ocean model (v3.1)[54] at a horizontal resolution of 9 km at the equator and a tripolar ORCA12 grid[55] were compared with *in situ* surface measurements. The comparisons were made for measurements taken between December 2018 and March 2020. The NEMO modeling system uses two bathymetry products: it uses ETOPO1, which is a surface relief model on a 1-arcmin grid,[56] for deeper water (depth $>$ 300 m) and the interpolated General Bathymetric Chart of the Oceans (GEBCO08)[57] for shallower water (depth $<$ 200 m). A 7-day assimilation cycle[58] of reduced-order Kalman filter was applied to the three-dimensional (3D) multivariate model, which itself was calculated from a singular extended evolutive Kalman (SEEK) filter.[59] The model large-scale temperature and salinity biases were calibrated in a 3D-var scheme, and *in situ* and RS salinity and temperature profiles were used to set the initial conditions in the model. For more details on this assimilation cycle and 3D-var scheme, see Lellouche et al.[58]

To compare ocean model output with *in situ* observations from January 2016 to February 2016, another daily 3D global ocean forecasting product from a coupled ocean-atmosphere system, also distributed by CMEMS,[60] was used. This model was produced by the Met Office (UK) and coupled (ocean-atmosphere) hourly to the NEMO ocean model (v3.4) with a resolution of 0.25 deg on the tripolar horizontal grid of ORCA025 (with a horizontal grid spacing of 28 km at the equator). The model dataset uses a daily updated 3D ocean analyses at an equirectangular projection in regular latitude and longitude, accompanied by 50 vertical levels down to 5500 m. Bathymetry from ETOPO1 and GEBCO was implemented in this coupled model as well. The model retained surface temperature and salinity through Haney retroaction, 3D Newtonian damping, and correction of the pressure gradient in the tropics (see Bell et al.,[61] for more details).

For this study, gridded daily mean values of model surface temperature (hereafter abbreviated as SST_{mod}) and surface salinity (SSS_{mod}) in the BoB were extracted from two model versions (described below) at 0.083 deg horizontal resolution in the continental shelf region of the BoB. In those cases where the high-resolution model data were not available (from January 2016 to February 2016), model output at 0.25 deg resolution was the only one used. These values of SST_{mod} and SSS_{mod} were then compared with *in situ* SST and SSS (see Sec. 2.2) and RS SST and SSS (see Sec. 2.3).

2.2 In Situ *Measurements*

In situ measurements of temperature, salinity, and density were acquired using a single-fire module with CTD probe (Sea and Sun Technology GmbH). This CTD probe is capable of measuring to 2000-m depth with a temperature accuracy of ± 0.002°C and a conductivity accuracy of ± 0.002 mS cm^{-1}.[62] The most recent CTD profiles were collected in three field sessions. The first session took place in January 2020, during a field expedition by the Department of Oceanography and Hydrography of Bangabandhu Sheikh Mujibur Rahman Maritime University (BSMRMU) aboard a fishing boat. The second session took place in February 2020, aboard the Bangladesh Navy Ship, the "*Sangu*." The final session took place in March 2020, where the profiles were obtained aboard fishing vessel "*Salman-2*."

These transects encompassed a total of 15 sites in both the eastern and western portions of the continental shelf region of the northern BoB (see Fig. 1). The cruises occurred over 3 months, and they sampled vertical depths down to 50 m. The raw CTD data were processed into a more user-friendly NetCDF format for efficient storage, usage, and sharing.[62] Vertical profiles of temperature and salinity were taken from this processed CTD data. In this study, only surface values

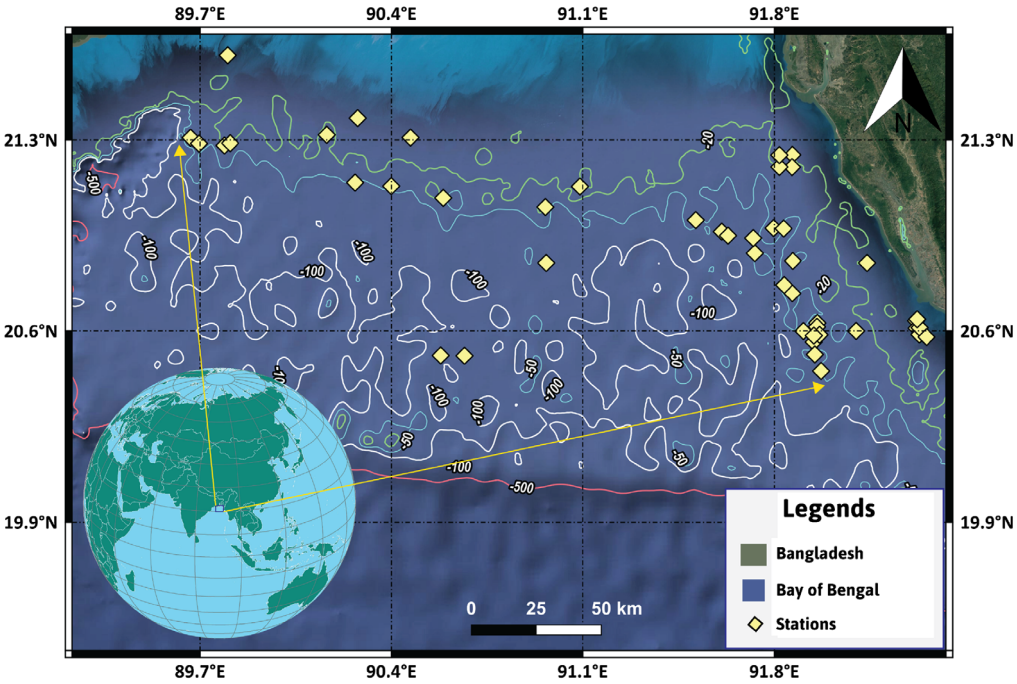

Fig. 1 Study area located in the northern IO (marked on the inset globe). The yellow diamonds represent the 46 sampling stations in the continental shelf of the northern BoB. Green, blue, white, and red contours represent the depth of 20, 50, 100, and 500 m, respectively.

of temperature and salinity were analyzed; a follow-up study is planned to compare subsurface temperature and salinity to model output. Another four CTD profiles were taken 1 year earlier, in December 2018, at the mouth of the Karnapahuli river estuary using the same single-fire module with CTD (Sea and Sun Technology GmbH). These four profiles were complemented by four more CTD profiles of temperature and salinity taken in December 2018 on the north, west, south, and east sides of St. Martin's Island.[63] Finally, 23 CTD profiles were obtained along 20.00°N to 21.20°N and 89.37°E to 92.20°E aboard the fishing vessel "*Agro food-4*" of Sea Resource Ltd. during a winter fishing period, and these profiles were taken between January 2016 to February 2016. Thus, a total of 46 measurements from CTD profiles from the northern BoB spanning the winter and spring months (December to March) from 2016 to 2020 were analyzed in this study.

2.3 *Satellite Observations*

Optimum Interpolation Sea Surface Temperature (OISST), also known as Reynolds SST, is the RS dataset used here for comparison. OISST (hereafter abbreviated as SST_{sat}) is a gridded product of 0.25 deg spatial resolution available daily.[64,65] These OISST values are interpolated from direct observations from the AVHRR. In both the model and satellite datasets, the grid values closest to the stations were considered representative of the station conditions. Similarly, both the model and satellite SST datasets were available daily, thus the daily value of each was compared with the *in situ* observations made on that day. Finally, although OISST is a hybrid product, including both satellite and *in situ* measurements, for the continental shelf area of the BoB, we are not aware of any *in situ* surface observations available for assimilation into the near real-time OISST product from January 2016 to March 2020 (the duration of our study). Thus, the OISST product analyzed here is primarily based on satellite observations.

Satellite salinity measurements were obtained from the global SSS L4 dataset, which was optimally interpolated onto a regular grid of 0.25 deg and later distributed by CMEMS. This salinity dataset[66] incorporates the near real-time European Space Agency's (ESA) SMOS product. High levels of noise generated during retrieval of SSS from satellites, along with substantial data gaps from clouds, were filled using a multidimensional optimal interpolation method. This interpolation was later validated from an *in situ* dataset.[67,68] Near real-time weekly SSS_{sat} values

Table 1 List of all the datasets used in this study, and their detailed information about the spatiotemporal resolution and processing level.

Product type	Product name	Production unit	Grid (deg)	Processing level	Temporal extent	Coverage
SST						
Model	Global Ocean 1/12° Physics Analysis and Forecast Updated Daily	Mercator Ocean	0.083	L4	Daily	July 2018 to Present
Model	Global Analysis and Forecasting Product from Coupled System	Met Office	0.25	L4	Daily	December 2015 to Present
Satellite	OISST	NOAA (AVHRR)	0.25	L4	Daily	September 1981 to Present
SSS						
Model	Global Ocean 1/12° Physics Analysis and Forecast Updated Daily	Mercator Ocean	0.083	L4	Daily	July 2018 to Present
Model	Global Analysis and Forecasting Product from Coupled System	Met Office	0.25	L4	Daily	December 2015 to Present
Satellite	Global Observed Ocean Physics Sea Surface Salinity Processing	Collected Localisation Satellites (CLS)	0.25	L4	Weekly	July 2018 to Present

were extracted from this product. Like the method used for SST, the average weekly value of SSS from satellite was matched to the model and *in situ* SSS values from the nearest grid-point value. All retrieved satellite and model temperature and salinity were gathered from open sources, and those are briefly summarized in Table 1.

2.4 *Quantifying Agreement between Datasets*

To investigate and quantify the agreement between the *in situ*, RS, and model values of SST and SSS, we calculated the Pearson correlation coefficient[69] using the following equation:

$$r = \frac{n\left(\sum xy\right) - \left(\sum x\right)\left(\sum y\right)}{\sqrt{\left[n\sum x^2 - \left(\sum x\right)^2\right]\left[n\sum y^2 - \left(\sum y\right)^2\right]}}, \tag{1}$$

where x, in our case, is *in situ* measurements and y is either model output or satellite observations. This method was used to calculate the correlation of (1) $\mathrm{SST_{in}}$ and $\mathrm{SSS_{in}}$ with (2) $\mathrm{SST_{mod}}$ and $\mathrm{SSS_{mod}}$ and (3) $\mathrm{SST_{sat}}$ and $\mathrm{SSS_{sat}}$. Additionally, scatter plots of these parameters were fitted to a linear model with a 95% significance level using the *ggpmisc* package in *R*.[70] Another commonly used metric, the RMSE, was calculated to quantify differences between model and satellite parameters (P_i) and the *in situ* values (O_i) using the *mltools* package[71] in *R*:

$$\mathrm{RMSE} = \sqrt{\frac{\sum_{i=1}^{n}(P_i - O_i)^2}{n}}. \tag{2}$$

In addition to RMSE, biases were calculated for the model and satellite parameters. The biases were calculated by following the method of Thakur et al.,[72] where the overlying grid values of both model and satellite datasets were subtracted from *in situ* observations in the corresponding grid. We calculated the standard deviation (SD) of the biases to depict overall variations for different locations and sources.

The index of agreement, or d-index, is a standardized measurement of error in model prediction that ranges between 0 and 1. A d-index of 1 implies a perfect match with the observations.[73] This index is capable of distinguishing proportional and additive differences of mean and variances of the simulated and observed values.[74] Here, we calculated d-indices between *in situ* (O_i) and satellite as well as model values (P_i). The following equation was used to calculate the d-index (md), using the *hydroGOF* package[75] in *R*:

$$md = 1 - \frac{\sum_{i=1}^{N} |O_i - S_i|^j}{\sum_{i=1}^{N} |S_i - \overline{O}| + |O_i - \overline{O}|^j}, \tag{3}$$

where O and S represent the observed and simulated values, respectively, and $\overline{O}$ is the mean of the observed values. Additionally, i represents the initial states of both parameters and j is the exponent applied in calculation of the d-index.

The final quantity used to assess the agreement between the *in situ* and model, and *in situ* and satellite, was the concordance correlation coefficient (CCC),[76] calculated using the *DescTools* package in *R*.[77] The CCC (ρ_c) represents precision, bias, and agreement with respect to a true value or magnitude of the observation coinciding with the concordance line.[78] The ρ_c quantifies biases and the fit with the concordance line

$$\rho_c = rC_b, \tag{4}$$

where the bias correction factor is given as C_b. The CCC thus depicts the deviation of the best-fit line, while r is the correlation coefficient between x and y. C_b is given as

$$C_b = \left[\frac{(\upsilon + 1/\upsilon + u^2)}{2}\right]^{-1}, \tag{5}$$

where υ and u represent the scale bias (slope shift) and location bias (height shift), respectively. These two terms can be expressed as

$$\upsilon = \frac{\sigma_1}{\sigma_2}, \tag{6}$$

$$u = \frac{\mu_1 - \mu_2}{\sqrt{\sigma_1 \times \sigma_2}}, \tag{7}$$

where μ_1 and μ_2 depict the means for the measurement and true values, respectively, and σ_1 and σ_2 represent their SDs. The CCC thus quantifies the magnitude of deviation of a dataset from a perfect agreement. CCC can be interpreted the same way as the Pearson's correlation coefficient, where values closer to 1 imply a stronger agreement with the observed value. CCC tends to be closer to zero than Pearson's correlation coefficient r.[79]

3 Results

3.1 *Statistical Comparison*

Scatter plots between *in situ* (SST_{in}) and satellite (SST_{sat}) [Fig. 2(a)], using the Student's t-test, show that model and *in situ* SST are positively correlated ($r = 0.82$, $p < 0.001$). We also used the Student's t-test to compare SST_{in} and SST_{mod} estimates [Fig. 2(b)], and these remain significantly correlated ($r = 0.77$, $p < 0.001$). In both cases, r values were statistically significant.

The mean bias and SD of bias for SST_{mod} were 0.43°C and 0.96°C, respectively (Table 2). For SST_{sat}, the SD of bias was larger (1.06°C) than it was for SST_{mod}, even though the mean bias decreased to 0.09°C. SST_{mod} and SST_{sat} had similar ranges of RMSE, 1.05°C and 1.07°C, respectively. Moreover, SST_{mod} and SST_{sat} had similar indices of agreement (d-indices) of 0.66 and 0.65. SST_{mod} and SST_{sat} agree well with the *in situ* measurements, with a model CCC of 0.92 and a satellite CCC of 0.95 (see Table 2).

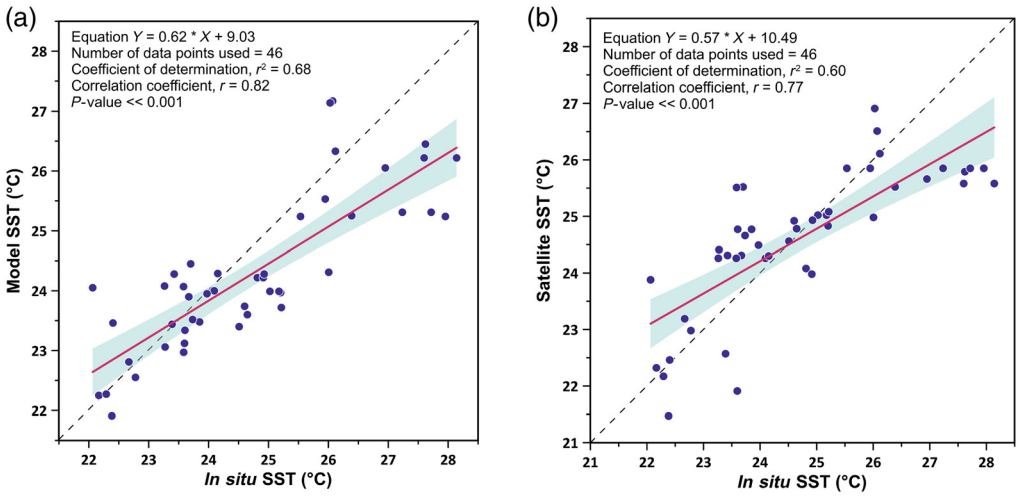

Fig. 2 Scatter plots of (a) *in situ* temperature versus model temperature, and (b) *in situ* temperature versus satellite temperature, showing the Pearson correlation coefficient (r) between SST_{mod} and SST_{sat} with SST_{in}. A regression line (red), based on a linear model, is drawn to show the best fit of the dataset, along with a semitransparent error bar (light green) showing a 95% confidence interval. P-value of the correlation coefficient is given.

Table 2 Summary table of all statistical analyses with the main results in this study.

Parameter	Mean	Correlation coefficient (r)	P-value	SD of bias	Mean of bias	RMSE	Index of agreement	CCC
SST_{mod}	24.3°C	0.82	<0.001	0.96	0.43°C	1.05°C	0.68	0.92
SST_{sat}	24.6°C	0.77	<0.001	1.06	0.09°C	1.07°C	0.65	0.95
SSS_{mod}	27.9 PSU	0.53	<0.001	1.99	2.74 PSU	3.38 PSU	0.31	0.45
SSS_{sat}	29.7 PSU	0.26	0.075	1.42	0.90 PSU	1.68 PSU	0.40	0.52

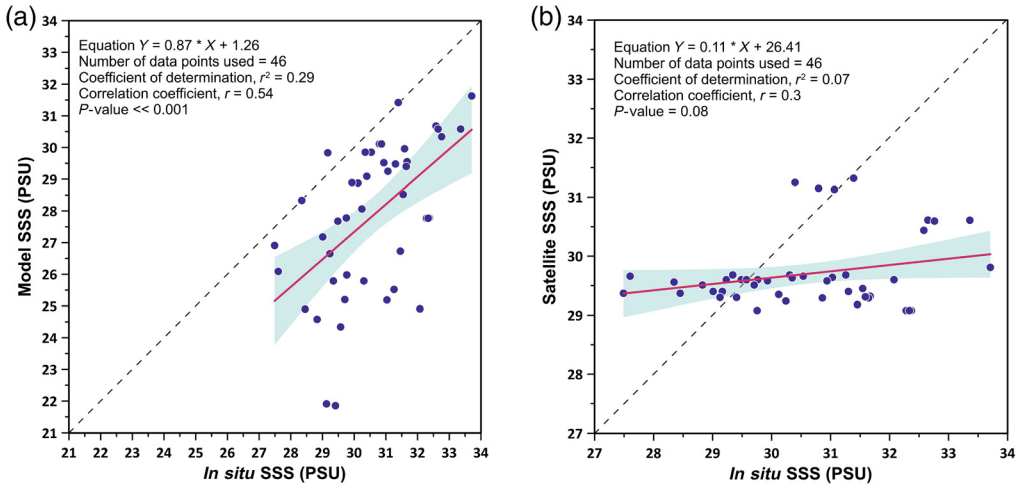

Fig. 3 As in Fig. 2, but for (a) *in situ* salinity versus model salinity, and (b) *in situ* salinity versus satellite salinity.

Unlike SST, which featured good agreement between *in situ* and both model and satellite, satellite (SSS_{sat}) and model (SSS_{mod}) SSS differed from *in situ* observations by an average of 1.84 PSU. SSS_{mod} was only weakly positively correlated with *in situ* measurements ($r = 0.54$), and SSS_{sat} was uncorrelated ($r = 0.26$) with *in situ* measurements [Figs. 3(a) and 3(b)].

The SSS_{mod} had a mean bias of +2.74 PSU when compared with *in situ* measurements. There was also large variance in SSS_{mod}, with a SD of 1.99 PSU (Table 2). The mean bias of SSS_{sat} was +0.90 PSU. The largest SD of the biases was 1.42 PSU, which was observed for SSS_{sat} (Table 2). Similarly, SSS_{mod} had a maximum RMSE of 3.38 PSU, whereas the RSME of the satellite was 1.68 PSU. This suggests that neither the model nor the satellite captured SSS well, and moreover, the model significantly underperformed the satellite. SSS_{mod} and SSS_{sat} had *d*-index values of only 0.31 and 0.40, respectively, indicating low agreement between both model and satellite and *in situ* SSS measurements. Additionally, both SSS_{mod} (CCC of 0.45) and SSS_{sat} (CCC of 0.52) had weaker concordance correlations than they did with SST. We discuss several possible reasons for the poor model performance in the next section.

3.2 *Spatial Variability in SST and SSS Biases*

Model SST products seem to have a positive bias. Most model SST grid points were overestimated by between +0.5°C and +2.7°C. This indicates that model SSTs were generally warmer than the observations [Fig. 4(a)]. The warm bias was strongest near the southeastern coastlines of the northern BoB, over the continental shelf region. While most of the model biases were warm, negative (cold) biases of relatively smaller magnitude (−1.0°C to −1.5°C) were also noticed in the study area. Fourteen station locations had small model SST biases (between −0.5°C and +0.5°C), and we consider those locations to be similar to the *in situ* measurements. While model SST biases were mostly positive, satellite SSTs [Fig. 4(b)] had predominately negative biases, ranging from −0.5°C to −1.5°C, with only six points depicting strong positive bias (+1.0°C to +2.7°C). Both positive and negative SST_{sat} biases did not have any distinct spatial pattern, and both were somewhat evenly dispersed on two fringes of the continental shelf of the bay. Overall, eight station locations had satellite SST small biases (between −0.5°C and +0.5°C).

The salinity analysis revealed both positive (i.e., salty) and negative (i.e., fresh) biases over the region. SSS_{mod} [Fig. 5(a)] had a mostly positive bias, with only three points having a negative bias. Most of the overestimations (24 stations) were between +0.5 and +4.0 PSU. The saltiest model overestimations (+4.0 to +7.5 PSU) were found in the eastern region of the study area. Model biases between −0.5 and +0.5 PSU were considered small, but unlike SST_{mod} where 14 stations had small biases, only two stations had small SSS_{mod} biases. SSS_{mod} featured a distinct longitudinal variation in bias, where the salinity overestimations occurred in the eastern BoB and underestimations occurred in the western BoB. In contrast to model salinity, the satellite salinity had an opposite pattern: a positive or saltier bias (+0.5 to +2 PSU) in the west and fresher or negative bias (−0.5 to −2.1 PSU) in the eastern areas of the study area [Fig. 5(b)]. Moreover, positive satellite SSS_{sat} salinity overestimations were generally much smaller in magnitude (<2 PSU) than the model biases, particularly in the eastern part of the BoB. Finally, SSS_{sat} had 12 stations with small over or underestimations (between −0.5 and +0.5 PSU).

4 Discussion

The primary goal of this study was to evaluate model and satellite SST and SSS products in the northern BoB. We accomplished that goal by comparing both model output and satellite measurements with *in situ* surface observations obtained during three cruises: January 2016 to February 2016, December 2018, and January 2020 to March 2020. To the best of our knowledge, this is the first comparative study using these recent datasets in this part of the BoB. Our results suggest that among all the products considered, the model and satellite SST products best matched with the *in situ* measurements over the northern BoB. However, model output and satellite measurements of salinity did not agree at all with the *in situ* observations over the northern BoB. Our results agree with other comparative studies performed in coastal areas, who also found low biases and high correlations between *in situ* SST and model and satellite SST[24,29] along with high biases and low correlations between *in situ* SSS and model and satellite SSS.[72]

Recent work suggests the introduction of new parameterizations in the NEMO model, such as additional dynamic height statistics and assimilations from several sources, can explain the agreement with *in situ* measurements.[80] Despite the reports of larger biases in SST_{sat} in different

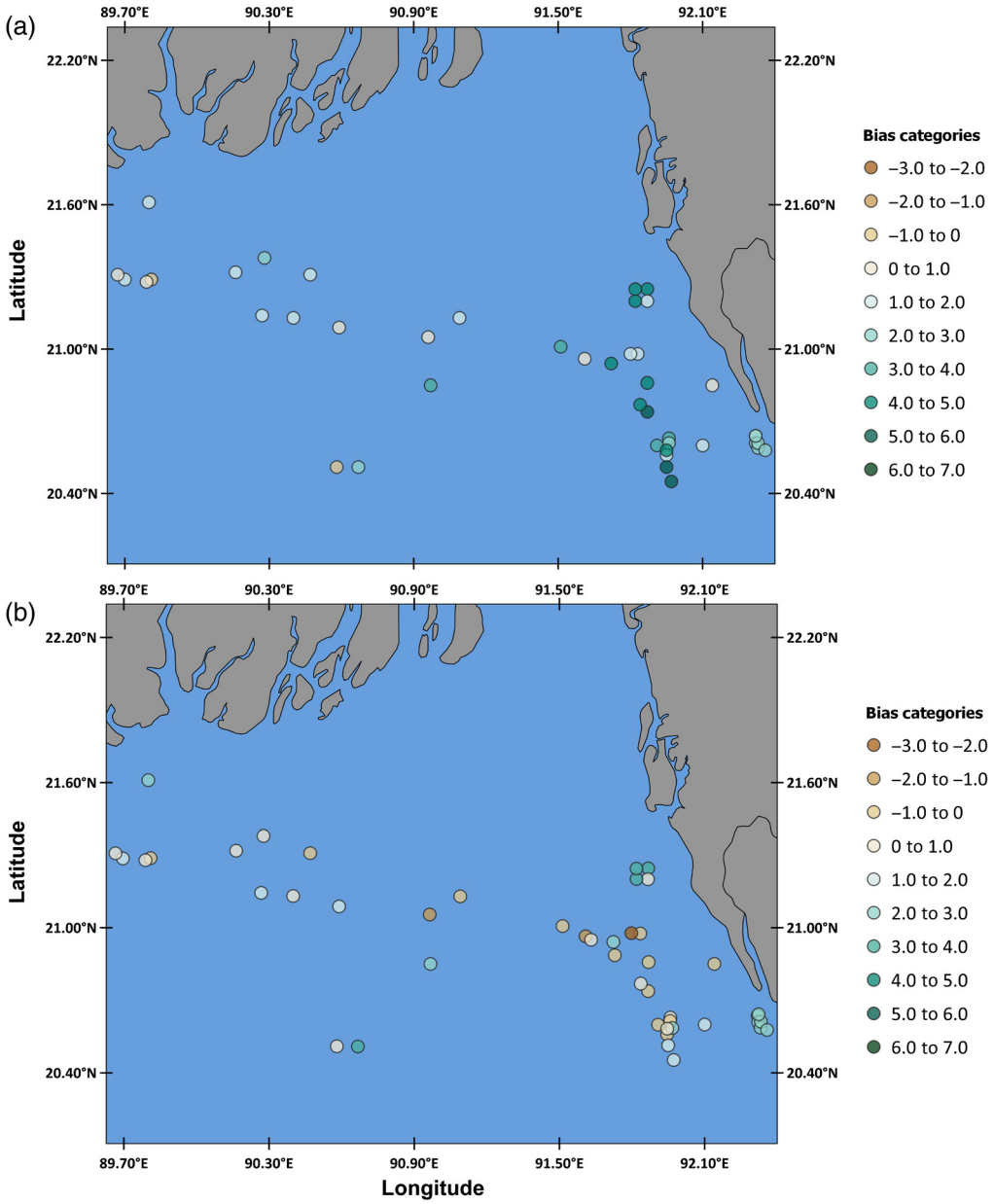

Fig. 4 The bias of (a) model and (b) satellite were compared with *in situ* measurements of SST over the continental shelf of the northern BoB. Points were categorically plotted where positive and negative biases are illustrated with red and blue points, accordingly. The deeper the corresponding color is, the higher the biases of corresponding color is.

shelf regions, including off the coasts of China,[81] South Africa,[82] the United States,[83,84] and Western Australia,[85,86] the continental shelf areas of the BoB features significantly smaller bias in SST_{sat}. Calculated model (0.68) and satellite (0.65) *d*-index values for SST in this study suggest both model and satellite SSTs agreed well with the *in situ* measurements made during the cruise. We found RMSE for SST_{mod} and SST_{sat} to be 1.05°C and 1.07°C, respectively, which are larger than the global average RMSE of 0.4°C calculated by Brasnett,[87] but smaller than the values (1.5°C) reported by Chen and Hu.[88] The larger RMSE temperature values are possibly explained by small-scale horizontal temperature gradients not captured well by the model or resolved well by the satellite.[25] Steep gradients typically exist between the northern and southern part of the BoB,[89] and those are sometimes poorly represented in either satellite or model output. Indeed, the RSME was larger in regions where the climatological SST gradient is larger and smaller in regions where the gradient tends to be smaller. Nevertheless, the CCC calculation

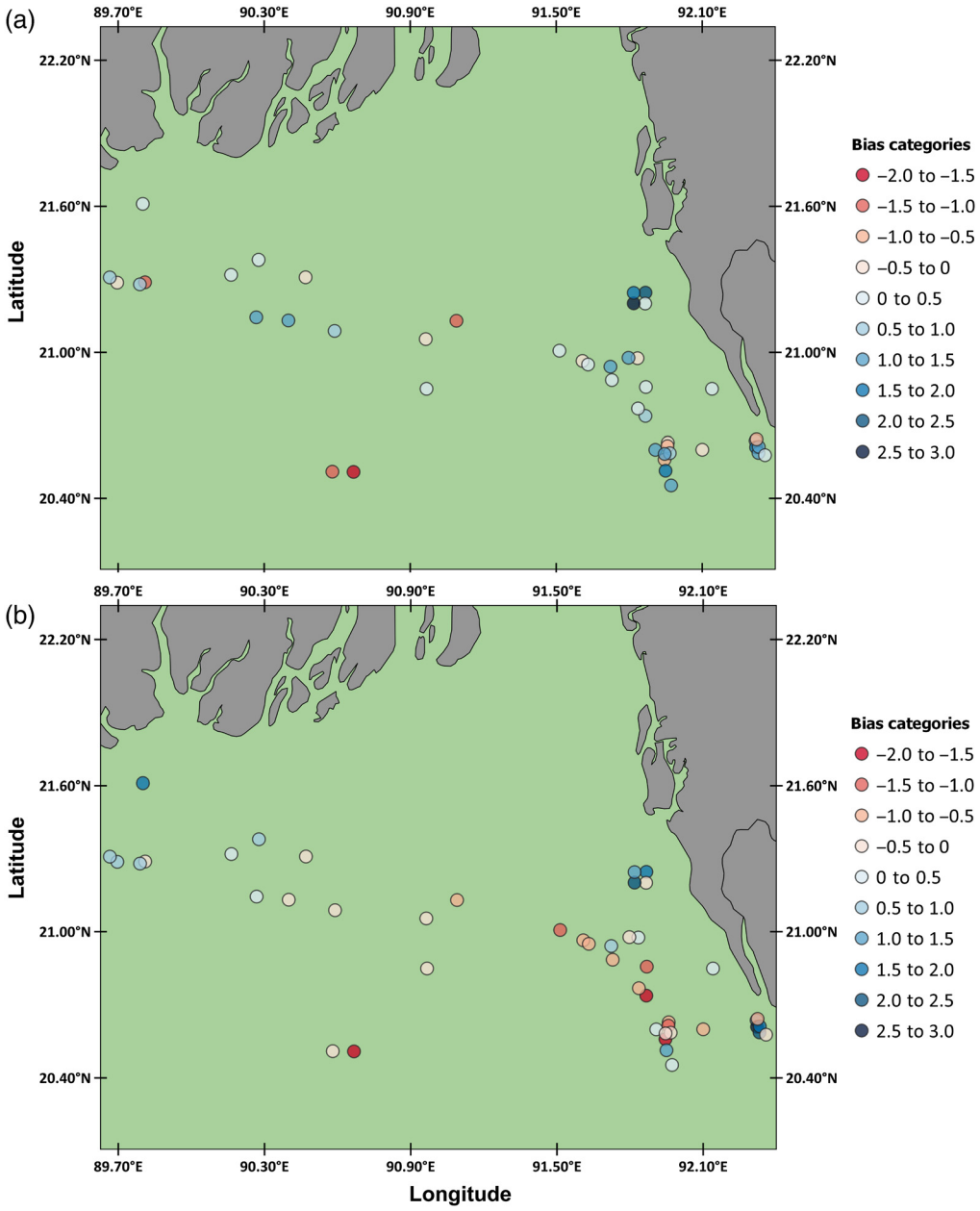

Fig. 5 As in Fig. 4, but for the bias of (a) model and (b) satellite SSS compared with *in situ* measurements, where positive and negative biases are represented by green and brown respectively.

affirmed that both SST_{mod} and SST_{sat} agreed with *in situ* SST: SST_{mod} (CCC = 0.92) and SST_{sat} (CCC = 0.92). This good fit could possibly be attributed to one of the inherent characteristics of the AVHRR satellite's IR sensor, as IR sensors can retrieve SST within 1 km of the coastline. Most of the stations in this study were more than 1 km from the coastline.

The diurnal cycle of SST over the ocean is relatively small because of seawater's large heat capacity.[90] Consideration of diurnal skin SST remains crucial for the tropics as it yields enhanced forecast.[91] Surface fluxes are subjectively affected by diurnal to intraseasonal scales due to the diurnal variability of skin SST.[92] All but two of the *in situ* measurements were made during the day, and those observations were then compared with the daily averaged model and satellite SST. Therefore, diurnal variability could have contributed to some of the differences between SST_{in} and SST_{sat}. Such diurnal variations have been reported in several regional seas, including the Mediterranean Sea,[93] Sargasso Sea,[94] equatorial tropical Pacific,[95] western North Pacific,[96] and western North Atlantic.[97] But, there has been very limited study of the diurnal variability of SST

in the BoB, and one such study suggests that the diurnal cycle is strong only during warming phases of the intraseasonal oscillations of SST.[98] Nevertheless, including the effects of the diurnal variation in the regional model algorithm would enhance the model's performance and coupling, as it would represent the air–sea interactions more accurately,[99] even on a longer time scale.[100]

Turning to SSS, *d*-index values for the model (0.31) and satellite (0.40) SSS suggested those datasets agreed only weakly with *in situ* cruise data. The RMSE increased to +3.4 PSU for SSS_{mod} and +1.7 PSU for SSS_{sat}. CCC values for SSS_{mod} and SSS_{sat} were low (0.45 and 0.52, respectively), confirming that both model and satellite SSS did not agree with the *in situ* measurements. The study area is subject to heavy freshwater influx from precipitation and river discharge, along with vertical stratification and horizontal advection. As such, high RMSE values for SSS products could be attributed to these physical processes, as they strongly affect general patterns of SSS and occur at scales that could be difficult to capture for both models and satellites. Furthermore, the radio frequency interference errors (ocean reflected radio frequency errors in passive microwave measurements) for RS products might be another possible cause for the SSS_{sat} disagreements with the *in situ* SSS.[101]

The coarse spatial resolution of the model and satellite products could also explain the disparities. It is known that ESA's SMOS data are often not suitable for coastal and estuarine studies as they can be too coarse at times.[30] This could be one of the many reasons for the differences between SSS_{sat} and SSS_{in}. Similar to the SST differences, it is also possible that the differences in SSS between *in situ* and model and satellite observations could be explained by temporal offsets between model (daily) and satellite (weekly values) and the instantaneous diurnal cycle sampled at the moment of the *in situ* SSS measurements. However, that would suggest that satellite values might be worse than model output, when the opposite was found here. The annual influx of 1300 km^3 of freshwater from the Ganga–Meghna–Brahmaputra river system[102] causes very large fluctuations in the surface salinity in the continental shelf seas of the northern BoB, and those fluctuations could possibly occur on sub-weekly time scales. However, the freshwater fluctuations are not directly captured by the salinity model, thus forcing the model to rely upon pseudo-observations (climatological river-runoff) with a higher signal to noise ratio (see the processing manual for the SSS data by CMEMS for more details). Another possible reason for the deviation could be that model salinity parameterizations and satellite salinity retrieval algorithms were developed for open-ocean applications, rather than coastal sites. Correction for only the large-scale biases was performed in the numerical model, which possibly limited the applicability here. It must be mentioned that we are aware of no comprehensive studies on the variability of SSS in the continental shelf of the BoB. We suggest that further study is necessary, and particularly additional field campaigns are needed over the shelf region of the BoB where high freshwater influx and stratification are occurred.

To summarize, continental shelf areas in the BoB are data-poor regions, as no continuous or long-term physical parameter datasets are available for the region. The northern BoB remains a highly dynamic region, especially along the coast and shelf region. Coastal shelf basins are prone to high short-term sedimentation,[103] and moreover, surface hydrographic forcing, with daily to even hourly variations, regularly alters the oceanographic conditions of coastal zones.[104,105] These ever-shifting surface processes are, at present, better captured with *in situ* measurements than numerical models or by satellite retrieval algorithms. Nevertheless, *in situ* measurements are not always openly accessible and are expensive to arrange. Satellite and models can overcome these limitations and provide continuous physiochemical information on the continental shelf areas of the BoB, but they are only useful when they compare favorably with *in situ* measurements.

5 Conclusions

This study presents evidence that in the data-poor region of the northern BoB, satellite observations and model analyses compare well with *in situ* measurements of SST but poorly with *in situ* measurements of SSS. We suggest that differences in the SSS in both satellite products and model analyses can be reduced by increasing the number of *in situ* observations and increasing the resolution of satellite data to better constrain the model in this region. Field campaigns are needed to continue to gather *in situ* data in both the coastal and the open-ocean regimes of the

BoB. More *in situ* measurements would assist in improving models or satellite algorithms that would more accurately capture the physicochemical conditions in the BoB.

6 Appendix A

The *in situ* measurements used in this study was done through the CTD deployments on several different occasions in 2016, 2018, and 2020. The stations' information was given in the following table (Table 3).

Table 3 The list of the available information of bathymetry, weather conditions, and other metadata for the sampling sites used in this study.

St. No	Latitude (°E)	Longitude (°N)	Date (month date, year)	Time (GMT + 6)	Depth (m)	Tide	Weather condition
1	20.64	92.32	February 26, 2018	11:15 a.m.	1.82	High	Sunny
2	20.61	92.32	February 27, 2018	11:37 a.m.	2.32	High	Sunny
3	20.59	92.33	February 27, 2018	12:04 p.m.	2.07	High	Sunny
4	20.61	92.33	March 1, 2018	12:50 p.m.	0.16	Low	Sunny
5	21.25	91.87	December 22, 2018	09:26 a.m.	20.63	Low	Sunny
6	21.20	91.87	December 22, 2018	09:52 a.m.	23.17	Low	Sunny
7	21.20	91.82	December 22, 2018	01:52 p.m.	20.61	High	Sunny
8	21.25	91.82	December 22, 2018	02:31 p.m.	18.08	High	Partially cloudy
9	20.58	92.36	January 2, 2020	05:17 p.m.	7.18	High	Sunny
10	20.64	92.32	January 3, 2020	10:04 a.m.	11.60	Low	Sunny
11	20.51	90.67	February 7, 2020	2:29 p.m.	83.06	High	Partially cloudy
12	20.60	92.10	February 8, 2020	09:38 a.m.	28.90	Low	Sunny
13	21.31	90.47	February 9, 2020	11:06 a.m.	14.38	Low	Sunny
14	21.38	90.28	February 9, 2020	08:54 a.m.	4.79	High	Sunny
15	21.32	90.16	February 9, 2020	09:56 a.m.	26.57	Low	Sunny
16	21.29	89.81	February 9, 2020	11:57 a.m.	19.57	High	Sunny
17	21.29	89.70	February 9, 2020	04:42 p.m.	27.71	High	Sunny
18	21.61	89.80	February 9, 2020	03:50 p.m.	5.47	High	Sunny
19	20.85	90.97	February 9, 2020	11:18 a.m.	82.74	Low	Sunny
20	20.51	90.58	March 18, 2020	12:31 p.m.	90.41	Low	Sunny
21	20.85	92.14	March 19, 2020	11:53 a.m.	11.95	High	Sunny
22	20.98	91.83	March 19, 2020	06:07 p.m.	54.19	Low	Partially cloudy
23	21.13	91.09	March 21, 2020	10:45 a.m.	10.49	High	Sunny
24	20.96	91.61	January 18, 2016	12:10 p.m.	85.85	Low	Sunny
25	20.95	91.63	January 20, 2016	02:20 p.m.	79.01	High	Partially cloudy

Table 3 (*Continued*).

St. No	Latitude (°E)	Longitude (°N)	Date (month date, year)	Time (GMT + 6)	Depth (m)	Tide	Weather condition
26	20.89	91.73	January 21, 2016	04:50 p.m.	54.78	High	Sunny
27	20.56	91.95	February 2, 2016	11:45 a.m.	43.85	High	Sunny
28	20.74	91.87	January 25, 2016	05:25 p.m.	33.63	High	Sunny
29	21.01	91.51	January 23, 2016	11:05 a.m.	47.14	Low	Sunny
30	20.63	91.96	January 27, 2016	09:35 p.m.	28.98	High	Night
31	20.61	91.96	January 27, 2016	10:11 p.m.	20.07	High	Night
32	20.86	91.87	January 29, 2016	09:40 a.m.	15.38	High	Sunny
33	20.59	91.97	January 27, 2016	10:35 p.m.	15.38	High	Cloudy
34	20.77	91.84	January 30, 2016	10:45 a.m.	38.17	High	Sunny
35	20.45	91.97	January 27, 2016	11:40 a.m.	50.45	Low	Sunny
36	20.51	91.95	January 28, 2016	05:40 p.m.	51.93	Low	Partially cloudy
37	20.60	91.91	January 28, 2016	04:15 p.m.	54.05	Low	Partially cloudy
38	20.58	91.95	January 29, 2016	05:15 p.m.	25.04	High	Sunny
39	20.98	91.80	January 29, 2016	10:45 a.m.	27.67	High	Sunny
40	21.05	90.96	February 4, 2016	12:06 p.m.	36.29	Low	Sunny
41	21.31	89.67	February 5, 2016	10:55 a.m.	35.86	High	Sunny
42	21.28	89.79	February 5, 2016	11:47 a.m.	18.21	High	Sunny
43	21.13	90.40	February 6, 2016	04:36 p.m.	36.94	Low	Sunny
44	21.14	90.27	February 7, 2016	09:14 a.m.	62.53	Low	Sunny
45	21.09	90.59	February 8, 2016	01:29 p.m.	44.12	High	Sunny
46	20.94	91.72	February 11, 2016	10:05 a.m.	60.96	Low	Sunny

Acknowledgments

This research was partially performed under a project funded by the University Grants Commission (UGC) of Bangladesh and Bangabandhu Sheikh Mujibur Rahman Maritime University, Bangladesh, Reference no. BSMRMU/PG Research-255 (part-04)/19/563. Additionally, the authors appreciate the Vice-Chancellor of BSMRMU, Dean of the Faculty of Earth and Ocean Science, and Bangladesh Navy for arranging the ship used in the field campaign. Special thanks to the University of Georgia Skidaway Institute of Oceanography for supporting Rivero-Calle and Md. Masud-Ul-Alam and funding this work as an open-access article. We also acknowledge the anonymous reviewers for their valuable comments. No potential conflict of interest was reported by the authors.

Data and Code Availability Statement

The data and code that support the findings of this study are available from the corresponding author, Md. Masud-Ul-Alam, upon request.

References

1. M. Foreman et al., "The ability of hydrodynamic models to inform decisions on the siting and management of aquaculture facilities in British Columbia," *DFO Can. Sci. Advis. Sec. Res.* **5**(7), 49 (2015).
2. J. W. Brown, O. B. Brown, and R. H. Evans, "Calibration of advanced very high resolution radiometer infrared channels: a new approach to nonlinear correction," *J. Geophys. Res. Ocean.* **98**(C10), 18257–18268 (1993).
3. A. Kumar et al., "Analysis of Pathfinder SST algorithm for global and regional conditions," *J. Earth Syst. Sci.* **109**(4), 395–405 (2000).
4. J. Vazquez-Cuervo, J. Gomez-Valdes, and M. Bouali, "Comparison of satellite-derived sea surface temperature and sea surface salinity gradients using the Saildrone California/Baja and North Atlantic Gulf Stream Deployments," *Remote Sens.* **12**(11), 1839 (2020).
5. T. G. Jensen et al., "Modeling salinity exchanges between the equatorial Indian Ocean and the Bay of Bengal," *Oceanography* **29**(2), 92–101 (2016).
6. R. Benshila et al., "The upper Bay of Bengal salinity structure in a high-resolution model," *Ocean Model.* **74**, 36–52 (2014).
7. S. V. Babu and A. D. Rao, "Mixing in the surface layers in association with internal waves during winter in the northwestern Bay of Bengal," *Nat. Hazards* **57**(3), 551–562 (2011).
8. A. Valsamidis and D. E. Reeve, "A new approach to analytical modelling of groyne fields," *Cont. Shelf Res.* **211**, 104288 (2020).
9. G. S. Bhat, G. A. Vecchi, and S. Gadgil, "Sea surface temperature of the Bay of Bengal derived from the TRMM microwave imager," *J. Atmos. Ocean. Technol.* **21**(8), 1283–1290 (2004).
10. S. Bojinski et al., "The concept of essential climate variables in support of climate research, applications, and policy," *Bull. Am. Meteorol. Soc.* **95**(9), 1431–1443 (2014).
11. J. Ferreira et al., "Progressing aquaculture through virtual technology and decision-support tools for novel management," in *Global Conf. Aquacult.*, pp. 643–704 (2012).
12. M. Dhanya and A. Chandrasekar, "Multivariate background error covariances in the assimilation of SAPHIR radiances in the simulation of three tropical cyclones over the Bay of Bengal using the WRF model," *Int. J. Remote Sens.* **39**(1), 191–209 (2018).
13. S. Horning et al., *Remote Sensing for Ecology and Conservation*, Oxford University Press, New York (2010).
14. M. Yang et al., "Analysis of the monthly and spring-neap tidal variability of satellite Chlorophyll-a and total suspended matter in a turbid coastal ocean using the DINEOF method," *Remote Sens.* **13**(4), 632 (2021).
15. N. Rascle et al., "Monitoring intense oceanic fronts using sea surface roughness: satellite, airplane, and in situ comparison," *J. Geophys. Res. Ocean.* **125**(8), e2019JC015704 (2020).
16. P.-Y. Le Traon et al., "Use of satellite observations for operational oceanography: recent achievements and future prospects," *J. Oper. Oceanogr.* **8**(suppl1), s12–s27 (2015).
17. R. T. Pinker et al., "Annual and seasonal variability of net heat flux in the northern Indian Ocean," *Int. J. Remote Sens.* **41**(17), 6461–6483 (2020).
18. A. Cracknell, *Advanced Very High Resolution Radiometer AVHRR*, CRC Press (1997).
19. M. J. Murray et al., "Direct observations of skin-bulk SST variability," *Geophys. Res. Lett.* **27**(8), 1171–1174 (2000).
20. Y. Kurihara et al., "A quasi-physical sea surface temperature method for the split-window data from the Second-generation Global Imager (SGLI) onboard the Global Change Observation Mission-Climate (GCOM-C) satellite," *Remote Sens. Environ.* **257**, 112347 (2021).
21. K. Hosoda and F. Sakaida, "Global daily high-resolution satellite-based foundation sea surface temperature dataset: development and validation against two definitions of foundation SST," *Remote Sens.* **8**(11), 962 (2016).
22. Barcelona Expert Center, "SMOS-BEC ocean and land products description. BEC-SMOS-0001-PD, Version 1.15," Barcelona (2016).
23. J. J. Kennedy et al., "Reassessing biases and other uncertainties in sea surface temperature observations measured in situ since 185: 1. Measurement and sampling uncertainties," *J. Geophys. Res. Atmos.* **116**(14), D14104 (2011).

24. K. D. Castillo and F. P. Lima, "Comparison of in situ and satellite-derived (MODIS-Aqua/Terra) methods for assessing temperatures on coral reefs," *Limnol. Oceanogr. Methods* **8**(3), 107–117 (2010).
25. Y. Wu et al., "A comparative study of satellite-based operational analyses and ship-based in-situ observations of sea surface temperatures over the eastern Canadian shelf," *Satell. Oceanogr. Meteorol.* **1**(1), 29–38 (2016).
26. B. Stobart et al., "Comparison of in situ and satellite sea surface-temperature data from South Australia and Tasmania: how reliable are satellite data as a proxy for coastal temperatures in temperate southern Australia?" *Mar. Freshwater Res.* **67**(5), 612 (2016).
27. S. Pramanik et al., "Interannual variability of the Chlorophyll-a concentration over Sri Lankan Dome in the Bay of Bengal," *Int. J. Remote Sens.* **41**(15), 5974–5991 (2020).
28. X. Lin et al., "Assessment of Aquarius sea surface salinity with Argo in the Bay of Bengal," *Int. J. Remote Sens.* **40**(22), 8547–8565 (2019).
29. A. J. Smit et al., "A coastal seawater temperature dataset for biogeographical studies: large biases between in situ and remotely-sensed data sets around the coast of South Africa," *PLoS One* **8**(12), Ie81944 (2013).
30. E. A. Urquhart et al., "Remotely sensed estimates of surface salinity in the Chesapeake Bay: a statistical approach," *Remote Sens. Environ.* **123**, 522–531 (2012).
31. J. L. Mueller et al., "Ocean optics protocols for satellite ocean color sensor validation, Revision 4, Volume I: Introduction, background and conventions," NASA/TM-2003-21621, p. 56 (2003).
32. J. Narvekar and S. Prasanna Kumar, "Seasonal variability of the mixed layer in the central Bay of Bengal and associated changes in nutrients and chlorophyll," *Deep. Res. Part I Oceanogr. Res. Pap.* **53**(5), 820–835 (2006).
33. M. Mahupratap et al., "Biological productivity characteristics in the Bay of Bengal," *Bay Bengal Process Stud.* **4**(1), 30–50 (2006).
34. J. D. Milliman and J. P. M. Syvitski, "Geomorphic/tectonic control of sediment discharge to the ocean: the importance of small mountainous rivers," *J. Geol.* **100**(5), 525–544 (1992).
35. M. Rahman et al., "Recent sediment flux to the Ganges-Brahmaputra-Meghna delta system," *Sci. Total Environ.* **643**, 1054–1064 (2018).
36. M. Masud-Ul-Alam et al., "Modeling spatio-temporal variability of suspended matter and its relation with hydrodynamic parameters in the northern Bay of Bengal," *Model. Earth Syst. Environ.* **7**, 2517–2530 (2020).
37. A. Morel, "Optical modeling of the upper ocean in relation to its biogenous matter content (case I waters)," *J. Geophys. Res.* **93**(C9), 10749 (1988).
38. R. Chester and J. Stoner, "Concentration of suspended particulate matter in surface sea water," *Nature* **240**(5383), 552–553 (1972).
39. L. Wen-Yao et al., "Measurement of the surface emissivity of turbid waters," *Remote Sens. Environ.* **21**(1), 97–109 (1987).
40. J. A. Wei et al., "The influence of increasing water turbidity on sea surface emissivity," *IEEE Trans. Geosci. Remote Sens.* **55**(6), 3501–3515 (2017).
41. P. D. Thorne, I. D. Lichtman, and D. Hurther, "Acoustic scattering characteristics and inversions for suspended concentration and particle size above mixed sand and mud beds," *Cont. Shelf Res.* **214**, 104320 (2020).
42. V. Rajamani et al., "Linking Indian rivers vs Bay of Bengal monsoon activity," *Curr. Sci.* **90**(1), 12–13 (2006).
43. A. Salahuddin et al., "Teleconnections between the sea surface temperature in the Bay of Bengal and monsoon rainfall in Bangladesh," *Global Planet. Change* **53**(3), 188–197 (2006).
44. D. Sengupta, B. R. Goddalehundi, and D. S. Anitha, "Cyclone-induced mixing does not cool SST in the post-monsoon north Bay of Bengal," *Atmos. Sci. Lett.* **9**(1), 1–6 (2008).
45. S. Neetu et al., "Influence of upper-ocean stratification on tropical cyclone-induced surface cooling in the Bay of Bengal," *J. Geophys. Res. Ocean.* **117**(12), C12020 (2012).
46. L. Yu, "Sea-surface salinity fronts and associated salinity-minimum zones in the tropical ocean," *J. Geophys. Res. Ocean.* **120**(6), 4205–4225 (2015).

47. S. Mathew et al., "Observed warming of sea surface temperature in response to tropical cyclone Thane in the Bay of Bengal," *Curr. Sci.* **114**(7), 1407–1413 (2018).
48. R. Venkatesan et al., "Analysis of drift characteristic in conductivity and temperature sensors used in Moored buoy system," *Ocean Eng.* **171**, 151–156 (2019).
49. M. I. J. Mili et al., "In-situ datasets of important physical and bio-chemical parameters in the continental shelf of the northern Bay of Bengal," *Data Brief* **35**, 106947 (2021).
50. R. Sundar et al., "Performance assessment of Indian Meteorological Ocean Buoys with INSAT telemetry," *Mar. Technol. Soc. J.* **50**(6), 33–39 (2016).
51. R. Venkatesan et al., "India's Ocean observation network: relevance to society," *Mar. Technol. Soc. J.* **50**(3), 34–46 (2016).
52. R. K. Sarangi et al., "Seasonal nitrate algorithms for the southwest Bay of Bengal water using in situ measurements for satellite remote-sensing applications," *J. Coast. Res.* **31**(2), 398–406 (2015).
53. S. Bhushan, A. F. Blumberg, and N. Georgas, "Comparison of NYHOPS hydrodynamic model SST predictions with satellite observations in the Hudson River Tidal, Estuarine, and Coastal Plume Region," in *Estuar. and Coast. Model. (2009)*, American Society of Civil Engineers, Reston, Virginia, Vol. 388, pp. 11–26 (2010).
54. G. Madec et al., "NEMO ocean engine," *Notes du Pôle modélisation l'Institut Pierre-Simon Laplace* **27**, 1–412 (2017).
55. G. Madec and M. Imbard, "A global ocean mesh to overcome the North Pole singularity," *Clim. Dyn.* **12**(6), 381–388 (1996).
56. C. Amante and B. Eakins, "ETOPO1 arc-minute global relief model: procedures, data sources and analysis," *NOAA Tech. Memo. NESDIS NGDC* **24**, 1–19 (2009).
57. J. J. Becker et al., "Global bathymetry and elevation data at 30 arc seconds resolution: SRTM30_PLUS," *Mar. Geod.* **32**(4), 355–371 (2009).
58. J.-M. Lellouche et al., "Recent updates on the Copernicus Marine Service global 1 ocean monitoring and forecasting real-time 1/12° high 2 resolution system," *Ocean Sci.* **14**, 1093–1126 (2016).
59. P. Brasseur and J. Verron, "The SEEK filter method for data assimilation in oceanography: a synthesis," *Ocean Dyn.* **56**(5–6), 650–661 (2006).
60. D. J. Lea et al., "Assessing a new coupled data assimilation system based on the met office coupled atmosphere-land-ocean-sea ice model," *J. ametsoc.org* **143**(11), 4678–4694 (2015).
61. M. J. Bell, M. J. Martin, and N. K. Nichols, "Assimilation of data into an ocean model with systematic errors near the equator," *Q. J. R. Meteorol. Soc.* **130**(598 part A), 873–893 (2004).
62. M. Masud-Ul-Alam et al., "An exclusive in-situ dataset on physicochemical parameters in the gappy northern Bay of Bengal," *Data Brief* **31**, 106024, (2020).
63. M. Kashem and A. S. Mahbub-e-kibria, "Assessment of Physico-chemical Status of Coastal Seawater of the Saint Martin's Island, Bangladesh," *Int. J. Sci. Eng. Res.* **10**(3), 84–91 (2019).
64. R. W. Reynolds et al., "Daily high-resolution-blended analyses for sea surface temperature," *J. Clim.* **20**(22), 5473–5496 (2007).
65. V. Banzon et al., "A long-term record of blended satellite and in situ sea-surface temperature for climate monitoring, modeling and environmental studies," *Earth Syst. Sci. Data* **8**(1), 165–176 (2016).
66. B. Nardelli and A. Pisano, "Quality information document for multi observation global ocean sea surface salinity and sea surface density product," *Mar. Environ. Monit. Serv.* (1), 4–23 (2020).
67. B. Buongiorno Nardelli, R. Droghei, and R. Santoleri, "Multi-dimensional interpolation of SMOS sea surface salinity with surface temperature and in situ salinity data," *Remote Sens. Environ.* **180**, 392–402 (2016).
68. R. Droghei, B. Buongiorno Nardelli, and R. Santoleri, "Combining in situ and satellite observations to retrieve salinity and density at the ocean surface," *J. Atmos. Ocean. Technol.* **33**(6), 1211–1223 (2016).
69. R Core Team, *R: A Language and Environment for Statistical Computing, 3.6.0*, R Foundation for Statistical Computing, Vienna, Austria. (2019).

70. P. J. Aphalo, "ggpmisc: miscellaneous extensions to 'ggplot2'," 0.3.5, Comprehensive R Archive Network (CRAN) (2020).
71. B. Gorman, "mltools: machine learning tools," 0.3.5 (2018).
72. K. K. Thakur et al., "Comparison of remotely-sensed sea surface temperature and salinity products with in situ measurements from British Columbia, Canada," *Front. Mar. Sci.* **5**(Apr.), 1–11 (2018).
73. C. J. Willmott, "On the validation of models," *Phys. Geogr.* **2**(2), 184–194 (1981).
74. D. R. Legates and G. J. McCabe, "Evaluating the use of 'goodness-of-fit' measures in hydrologic and hydroclimatic model validation," *Water Resour. Res.* **35**(1), 233–241 (1999).
75. M. Zambrano-Bigiarini, "hydroGOF: Goodness-of-fit functions for comparison of simulated and observed hydrological time series," 0.4-0 (2020).
76. L. I.-K. Lin, "A concordance correlation coefficient to evaluate reproducibility," *Biometrics* **45**(1), 255 (1989).
77. A. Signorell et al., "DescTools: tools for descriptive statistics," 0.99.37 (2020).
78. M. Nita, M. A. Ellis, and L. V. Madden, "Reliability and accuracy of visual estimation of phomopsis leaf blight of strawberry," *Phytopathology* **93**(8), 995–1005 (2003).
79. N. V. S. Yadav et al., "Development and validation of standard area diagrams to aid assessment of pecan scab symptoms on fruit," *Plant Pathol.* **62**(2), 325–335 (2013).
80. J. M. Lellouche et al., "Quality information document for global sea physical analysis and forecasting product," *E.U. Copernicus Mar. Serv. Inf.* **2.1**(April), 1–100 (2019).
81. D. L. Tang et al., "AVHRR satellite remote sensing and shipboard measurements of the thermal plume from the Daya Bay, nuclear power station, China," *Remote Sens. Environ.* **84**(4), 506–515 (2003).
82. F. Dufois et al., "On the warm nearshore bias in Pathfinder monthly SST products over Eastern Boundary Upwelling Systems," *Ocean Model.* **47**, 113–118 (2012).
83. C. A. Blanchette et al., "Biogeographical patterns of rocky intertidal communities along the Pacific coast of North America," *J. Biogeogr.* **35**(9), 1593–1607 (2008).
84. B. R. Broitman et al., "Climate and recruitment of rocky shore intertidal invertebrates in the Eastern North Atlantic," *Ecology* **89**(sp11), S81–S90 (2008).
85. D. Smale and T. Wernberg, "Satellite-derived SST data as a proxy for water temperature in nearshore benthic ecology," *Mar. Ecol. Prog. Ser.* **387**, 27–37 (2009).
86. A. Pearce, F. Faskel, and G. Hyndes, "Nearshore sea temperature variability off Rottnest Island (Western Australia) derived from satellite data," *Int. J. Remote Sens.* **27**(12), 2503–2518 (2006).
87. B. Brasnett, "The impact of satellite retrievals in a global sea-surface-temperature analysis," *Q. J. R. Meteorol. Soc.* **134**(636), 1745–1760 (2008).
88. S. Chen and C. Hu, "Estimating sea surface salinity in the northern Gulf of Mexico from satellite ocean color measurements," *Remote Sens. Environ.* **201**, 115–132 (2017).
89. A. K. Jaswal, V. Singh, and S. R. Bhambak, "Relationship between sea surface temperature and surface air temperature over Arabian Sea, Bay of Bengal and Indian Ocean," *J. Ind. Geophys. Union* **16**(2), 41–53 (2012).
90. G. Danabasoglu et al., "Diurnal coupling in the tropical oceans of CCSM3," *J. Clim.* **19**(11), 2347–2365 (2006).
91. S. Akella, R. Todling, and M. Suarez, "Assimilation for skin SST in the NASA GEOS atmospheric data assimilation system," *Q. J. R. Meteorol. Soc.* **143**(703), 1032–1046 (2017).
92. Y. Takaya et al., "Refinements to a prognostic scheme of skin sea surface temperature," *J. Geophys. Res. Ocean.* **115**(C6), 6009 (2010).
93. E. Böhm, S. Marullo, and R. Santoleri, "AVHRR visible-IR detection of diurnal warming events in the western mediterranean sea," *Int. J. Remote Sens.* **12**(4), 695–701 (1991).
94. J. F. Price et al., "Diurnal response of sea surface temperature observed at the long-term upper ocean study (34°N, 70°W) in the Sargasso Sea," *J. Geophys. Res.* **92**(C13), 14480 (1987).
95. A. Soloviev and R. Lukas, "Observation of large diurnal warming events in the near-surface layer of the western equatorial Pacific warm pool," *Deep. Res. Part I Oceanogr. Res. Pap.* **44**(6), 1055–1076 (1997).

96. S. Tanahashi et al., "Diurnal variations of sea surface temperature over the wide-ranging ocean using VISSR on board GMS," *J. Geophys. Res. Ocean.* **108**(C7), 3216 (2003).
97. P. Cornillon and L. Stramma, "The distribution of diurnal sea surface warming events in the western Sargasso Sea," *J. Geophys. Res.* **90**(C6), 11811 (1985).
98. M. Mujumdar et al., "Diurnal cycle induced amplification of sea surface temperature intra-seasonal oscillations over the bay of Bengal in summer monsoon season," *IEEE Geosci. Remote Sens. Lett.* **8**(2), 206–210 (2011).
99. S. Marullo et al., "The diurnal cycle of sea-surface temperature and estimation of the heat budget of the Mediterranean Sea," *J. Geophys. Res. Ocean.* **121**(11), 8351–8367 (2016).
100. S. Masson et al., "Impact of intra-daily SST variability on ENSO characteristics in a coupled model," *Clim. Dyn.* **39**(3), 681–707 (2012).
101. H. Y. Kao et al., "Assessment of aquarius sea surface salinity," *Remote Sens.* **10**(9), 1341 (2018).
102. D. Sengupta, G. N. Bharath Raj, and S. S. C. Shenoi, "Surface freshwater from Bay of Bengal runoff and Indonesian throughflow in the tropical Indian Ocean," *Geophys. Res. Lett.* **33**(22), 609 (2006).
103. P. J. Mitchell et al., "Sedimentation rates in the Baltic Sea: a machine learning approach," *Cont. Shelf Res.* **214**, 104325 (2021).
104. G. M. Fragoso et al., "Physical controls on phytoplankton size structure, photophysiology and suspended particles in a Norwegian biological hotspot," *Prog. Oceanogr.* **175**, 284–299 (2019).
105. G. M. Fragoso et al., "Phytoplankton community succession and dynamics using optical approaches," *Cont. Shelf Res.* **213**, 104322 (2021).

Md. Masud-Ul-Alam is a graduate student in the Department of Marine Science, University of Georgia, Athens. Additionally, he is a lecturer in oceanography at Bangabandhu Sheikh Mujibur Rahman Maritime University, Bangladesh. He started his career at the Physical and Space Oceanography Division, BORI, Bangladesh. He received his MS degree in oceanography from the University of Dhaka. He worked as a research fellow at AWI, Germany. His research interests include satellite oceanography, air–sea interactions, and ocean modeling.

Md. Ashif Imam Khan is a final year undergraduate student who majors in oceanography. He is currently performing a thesis upon paleo-climatic conditions during the Last Interglacial and Last Glacial Maximum in the BoB. His research interest lies in performing spatial and temporal analysis using remotely sensed and model datasets that incorporate physical, chemical, biological, and meteorological aspects of the ocean and atmosphere.

Bradford S. Barrett received his PhD in meteorology and has studied the intersection of climate, extreme events, and the ocean. His research spans multiple temporal and spatial scales, with focus on variability of the atmosphere, ocean, and cryosphere on the subseasonal scale.

Sara Rivero-Calle is an assistant professor at the University of Georgia. She received her BSc degree in biology from Complutense University, her MSc degree in biological oceanography from the University of Puerto Rico, and her PhD in oceanography from Johns Hopkins University. At UGA, she manages the Bio-Optical and Satellite Oceanography lab and is a science lead of SeaHawk CubeSat. She is interested in CubeSat Technology, subpixel variability, and the intersection of RS and numerical models.